Tissue Phantoms for Biomedical Applications in Raman Spectroscopy: A Review

Martha Z Vardaki and Nikolaos Kourkoumelis

Department of Medical Physics, School of Health Sciences, University of Ioannina, Ioannina, Greece.

Biomedical Engineering and Computational Biology
Volume 11: 1–15

DOI: 10.1177/1179597220948100
SAGE

ABSTRACT: Raman spectroscopy is a group of analytical techniques, currently applied in several research fields, including clinical diagnostics. Tissue-mimicking optical phantoms have been established as an essential intermediate stage for medical applications with their employment from spectroscopic techniques to be constantly growing. This review outlines the types of tissue phantoms currently employed in different biomedical applications of Raman spectroscopy, focusing on their composition and optical properties. It is therefore an attempt to present an informed range of options for potential use to the researchers.

KEYWORDS: Raman spectroscopy, tissue phantoms, optical properties, biomedical applications

RECEIVED: April 10, 2020. **ACCEPTED:** July 16, 2020.

TYPE: Review

FUNDING: The author(s) disclosed receipt of the following financial support for the research, authorship, and/or publication of this article: This research is co-financed by Greece and the European Union (European Social Fund- ESF) through the Operational Programme "Human Resources Development, Education and Lifelong Learning" in the context of the project "Reinforcement of Postdoctoral Researchers - 2ndr Cycle" (MIS-5033021), implemented by the State Scholarships Foundation (ΙΚΥ).

DECLARATION OF CONFLICTING INTERESTS: The author(s) declared no potential conflicts of interest with respect to the research, authorship, and/or publication of this article.

CORRESPONDING AUTHOR: Martha Z Vardaki, Department of Medical Physics, School of Health Sciences, University of Ioannina, 45110 Ioannina, Greece.
Email: martha.vardaki@msl.ubc.ca

Introduction

Raman spectroscopy (RS) is a group of techniques based around the analysis of inelastic (Raman scattered) light resulting from the interaction between light and matter. Raman scattered light provides information on the molecular bond vibrations, which can be exploited for the acquisition of sample-specific molecular fingerprints. Due to its non-invasive nature, Raman spectroscopy has been employed in different modes to address various biomedical issues over the last few decades. Some of them include cancer screening,[1] pathogen identification,[2,3] body fluid analysis,[4] transfusion blood assessment,[5] disease diagnosis,[6-8] drug analysis,[9] or even as a process analytical tool for cell therapies.[10]

The continuous need for tissue-like samples in the standardization and development of spectroscopic and other optical applications combined with the limited availability of human tissue due to ethics reasons, has led to the adoption of tissue-mimicking phantoms or *tissue models*. The optical tissue phantoms are synthetic models mimicking not only human tissue properties, but also light propagation and interactions through it. This presents a significant quality for spectroscopic techniques, which have recruited tissue phantoms over time for (a) feasibility and reproducibility testing, (b) optimization, and (c)calibration reasons.

Tissue phantoms are essentially diffuse matrices of various composition, geometry, and optical properties. They exist in many different forms but are generally divided into those of solid, hydrogel, and liquid state. Their common feature is that absorption, scattering, and other optical properties can be controllably modeled during fabrication. A different category of tissue phantoms is the ex vivo animal tissue, which is often used in spectroscopy studies for a more realistic approach. Although animal phantoms cannot be easily controlled in terms of optical properties, they provide an inherent heterogeneity in tissue composition which is very similar to the human one.

The flexibility and properties of tissue phantoms have rendered them an important part of technology development and translation process. Over the past few decades, tissue phantoms have been extensively used for ex vivo measurements preceding the implementation of any optical technique in clinical settings.[11] In this review, we attempt to outline most of the tissue phantoms employed for biomedical applications in Raman spectroscopy, focusing on three different aspects: (a) most commonly used tissue phantom types, (b) phantom design, and (c) biomedical applications in the field of Raman spectroscopy involving optical tissue phantoms. We hope that this review will inform researchers on the current applications of synthetic and animal tissue phantoms, facilitating their choice in future research.

Types of Phantoms

The most commonly used phantoms are liquid tissue phantoms, solid silicone or polymer phantoms, gelatin/ agarose phantoms, and animal phantoms (Figure 1). As the different types of phantoms have been extensively described in comprehensive reviews before,[12-14] they are only briefly mentioned below.

Liquid tissue phantoms are the easiest and most flexible in fabrication, as they can be easily controlled and managed in terms of volume and consistency. Because of the latter, the optical properties of liquid phantoms can be adjusted just by changing the relative proportions of absorbing and scattering agents in the phantom solution. The liquid phantoms are commonly made of mixing a commercially available lipid emulsion (Intralipid, Liposyn) and added absorber (eg, ink) in a container. The container material may vary depending on the

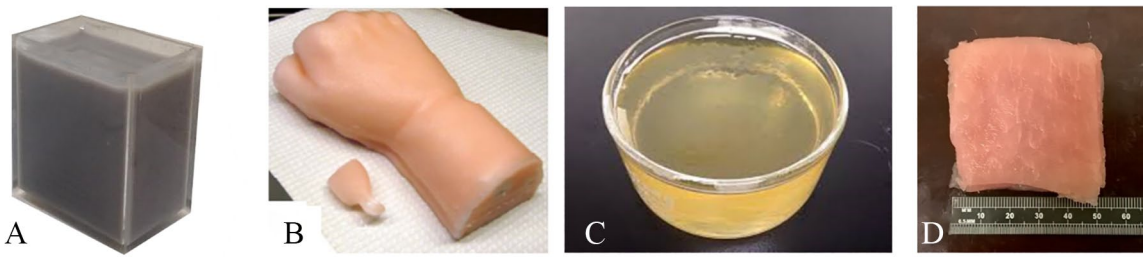

Figure 1. Examples of simple tissue phantoms: (A) liquid tissue phantom, (B) solid tissue phantoms of a human wrist and rat leg,[14] (C) gelatin phantom (reproduced with permission),[15] and (D) animal tissue phantom. (A and D are images from the authors' unpublished work).

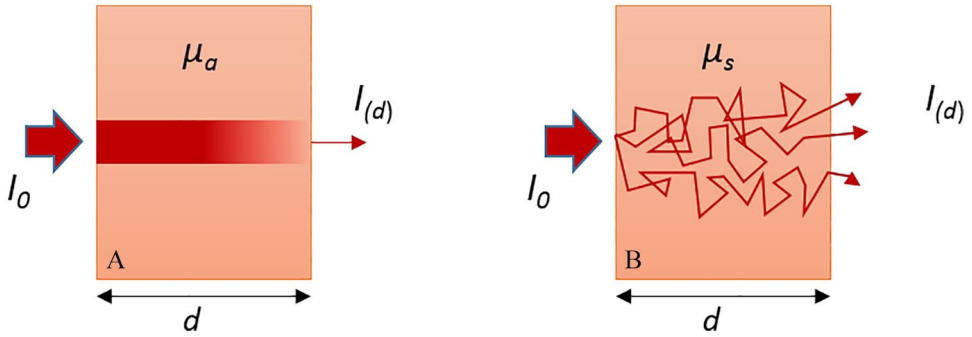

Figure 2. Transmission of light through an absorbing (A) and diffusely scattering (B) medium.[19]

application and the possibility of light reaching the container walls. The liquid nature of the phantoms allows for significant flexibility in sample measurements, such as incorporation of Raman scattering or fluorescence features, even after the fabrication process has been completed. Another major advantage of liquid phantoms over the solid ones is the uncomplicated and rapid synthetic procedure.

On the other hand, solid phantoms can be time-consuming and not flexible in fabrication, as their optical properties cannot easily change by adding or removing components to the matrix. Solid phantom samples have been made using bulk matrices of different degrees of transparency, such as polymers, silicone, and wax. Although polymer-based phantoms have been reported to be sometimes instable in size during polymerization,[16] they are generally considered to be preserved better and for a longer period of time compared to animal tissue or liquid tissue phantoms. A special category of semi-solid tissue phantoms are the hydrogel-based ones, including agarose and gelatin matrices. Both phantom types have been extensively used for imaging[12] and assessed for biocompatibility.[17] Since hydrogel phantoms contain water as their main component, evaporation of the solvent can take place, changing the dimensions and optical properties of the phantom within a short period of time. As such phantoms are also prone to bacterial growth, preservatives may be used for lifetime extension.

Animal phantoms are the most realistic choice as they accurately simulate the heterogeneity, mechanical properties, and consistency of the human tissue. Ex vivo animal tissue is commonly used in Raman spectroscopy not only for their intrinsic scattering and absorbing properties but also for their morphology and chemical composition. In combination with their morphological complexity and presence of autofluorescence induced by chromophores which are also found in human tissue, ex vivo animal tissue can serve as a highly accurate model for light propagation.[18] Despite their benefits, animal tissue phantoms are difficult to be controlled in terms of sample composition for reproducible measurements as their optical properties cannot be adjusted precisely. In addition, reduced tissue absorption is expected in the excised animal tissues, due to decrease in blood volume during removal. However, animal phantoms are useful as an intermediate stage prior to human or in vivo animal studies, as they allow researchers to investigate healthy and diseased tissues in ways that would be inaccessible in a human patient due to ethics.

Phantom Design

Optical properties

While photons propagate through tissues, they are being scattered or absorbed by the tissue molecules. During scattering, which is more commonly taking place at interfaces of tissue components with different refractive indices, light photons interact with matter and change their direction, with (inelastic scattering) or without (elastic or diffuse scattering) losing energy. The more scattering the medium is, the more the photons will deviate from the original forward direction (Figure 2). In the case of absorption, the photons will be absorbed only when the energy of the photon matches the energy gap between the initial and the final energy states of the atom or molecule. How efficiently the photon will travel through the tissue, depends on the fraction of light which will be absorbed or scattered by it, which is described principally by the scattering and absorption coefficients. In biological tissues, absorption and

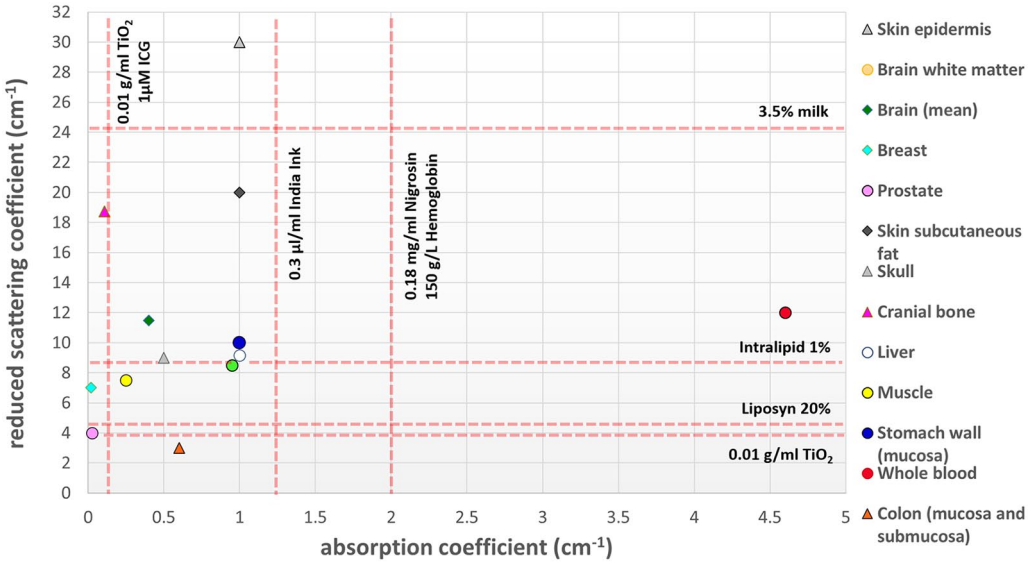

Figure 3. Reduced scattering and absorption coefficients for typical concentrations of scattering and absorbing agents commonly used in tissue phantom fabrication, in comparison with optical properties of different types of healthy human tissues at 830 nm.

scattering are commonly taking place in the same sample with the effect of absorption to be much stronger than one would expect as a result of the extra optical path length.

The scattering coefficient (μ_s) depends on the probability of the medium per unit length to redirect the incident photons into new directions and therefore prevent the forward on-axis transmission of light. The average distance that a photon travels between scattering events is called mean free path length. Similarly, the absorption coefficient (μ_α) describes the probability of the medium per unit length to absorb the photons.[20] Because in biological tissues the light is not scattered in all possible directions but is mainly forward directed (anisotropic scattering),[21,22] it is convenient to define a mean scattering angle which is described by the value of anisotropy (g).[23] To be more precise in the description of scattering in biological tissues, scattering coefficient and anisotropy are combined into the expression of reduced scattering coefficient (μ'_s) which is defined as

$$\mu'_s = \mu_s (1 - g) \quad (1)$$

The optical properties described above (μ_α, μ_s, μ'_s and g) are characteristic of tissue and vary for different types of human tissue. To appropriately simulate visible or infrared light propagation in a certain tissue, it is necessary to reproduce its optical properties at the measuring wavelength. By replicating optical properties, we simulate co-dependent parameters such as the concentration of various chromophores inside the tissue (absorption coefficient), and the form, size and concentration of the scattering components in the tissue (scattering coefficient).[24]

Commonly used scatterers for the fabrication of tissue phantoms include fat emulsions such as Intralipid and Liposyn, milk, TiO_2, latex, and polystyrene microspheres. Absorbing media include different types of inks (India ink, black ink, red ink), dyes (blue dye, naphthol green dye, nigrosin, indocyanine green), and biological absorbers (hemoglobin, β-carotene, melanin). The desirable optical properties in the phantom volume can be achieved by mixing the correct proportions of scattering and absorbing agent.

Below we present typical concentrations of scatterer and absorber media, commonly used in tissue phantom fabrication, in correlation with the optical properties of characteristic human tissues (Figure 3). The reduced scattering and absorption coefficients are based on experimental data of healthy human tissue at 830 nm for different skin layers,[25] brain,[26,27] breast,[28] cranial bone,[29] liver,[30] muscle,[31] stomach wall mucosa,[32] colon,[33] prostate,[34] skull,[26] and whole blood.[35] Optical properties of the scattering and absorbing media included in the plot were also derived from the literature for nigrosin,[36] TiO_2,[37] milk,[38] Liposyn,[39] hemoglobin,[40] indocyanine green (ICG),[39] Intralipid,[41] and India ink.[42] The exact values used in the figure can be found in Supplementary Material (S1).

Geometry and chemical composition

Even if a phantom exhibits optical properties equivalent to a certain tissue, the morphology of the phantom is a significant feature to match the tissue in terms of the anatomical shape. For cases where feasibility evaluation of a spectroscopic technique is required, the macroscopic geometry of the sample should be ideally reproduced in the tissue phantom.

Another prerequisite for the phantoms to fully simulate the respective tissue is to match the chemical properties. This is especially important in Raman spectroscopy because of the sensitivity of the technique to tissue chemistry on a molecular level. The chemical composition of a tissue is particularly challenging to reproduce in a phantom. This has led to the introduction of ex vivo animal tissue, or *animal phantoms*.

Table 1. Types and characteristics of tissue phantoms in Raman spectroscopy studies with a focus on biomedical applications.

AUTHORS	PHANTOM TYPE	MATRIX/ CONTAINER	SCATTERER	ABSORBER	PROBING	RS MODALITY	WAVELENGTH (NM)	SIMULATED TISSUE/ PURPOSE OF THE STUDY
Chuchuen et al[113]	Liquid	Agarose	Intralipid	–	Siliconwafer	Confocal RS	785	Depth of focus estimation
Maher and Berger[114]	Liquid	–	Dairy creamer and teflon		Ratio of 2 layers	SORS	830	Optimum offset determination
McCain et al[115,116]	Liquid	Cuvette	Intralipid	–	ethanol	Multimodal multiplex RS	808	System evaluation
Dingari et al[74]	Liquid	–	Intralipid	India ink	Added glucose	Conventional RS	830	Blood/Study of signal variations
Vardaki et al[42,63]	Liquid	Quartz cuvette	Intralipid	India ink	*trans*-stilbene/HAP	Transmission RS	830	Prostate, breast/ detecting origin of Raman signal within sample volume
Motz et al[117]	Liquid	Glass vial	Latex microspheres	Hb, India ink	Added sodium perchlorate	Optical fiber Raman probe	830	Arterial tissue/ System evaluation
Dingari et al[78]	Liquid	Fused silica cuvette	Intralipid	India ink	Added glucose/ creatinine	Conventional RS	830	Blood/ System Calibration/ wavelength selection
Barman et al[75]	Liquid	Fused silica cuvette	Intralipid	India Ink	Glucose (plus creatinine)	Turbidity corrected RS	830	Blood/ System evaluation and calibration
Barman et al[79]	Liquid	Water in container	Indocyanine green (fluorescence agent) and urea		Added glucose	Shifted subtracted RS	830	Blood/ System evaluation/ Photobleaching assessment
Maher et al[118]	Liquid	–	PS microspheres, PDMS, Intralipid	India ink	Ratio of 2 layers	Confocal RS + OCT	785	Esophageal tissue/ Determination of axial resolution
Gardner et al[66]	Liquid	Quartz	Intralipid	India ink	PTFE layer	TRS based on differential transmittance	830	Breast/ Depth prediction of lesion
Iping Petterson et al[119]	Liquid	Petri dish	Intralipid	India ink	PTFE	Multifibre Raman probe inside a hypodermic needle	830	Lymph nodes/ System evaluation
Zavaleta et al[120]	Liquid	Water	Lipid	India ink	SWNTs	Raman microscope	785	Evaluation of maximum penetration depth for SERS
Zavaleta et al[121]					SERS NPs in agar	Endoscope		
Brenan and Hunter[122]	Liquid	Water	Milk	–	Wax film	Confocal RS	488	Evaluation of the system spatial resolution
Agenant et al[123]	Liquid	–	Intralipid	–	PET	Raman probe	785	System evaluation (depth response) for epithelial tumor detection
Karpienko et al[83]	Liquid	Isotonic saline	Blood derivative (plasma substitution)		–	Conventional RS	830	Blood/ Evaluations of the phantoms
Bechtel et al[77]	Liquid	Water	Intralipid	India ink	Glucose, creatinine	Intrinsic RS	830	System evaluation
Schulmerich et al[44]	Hydrogel	Agarose	Intralipid	–	Teflon	Raman tomography	785	Bone/ CT data calibration
Demers et al[49]	Hydrogel	Agarose	Intralipid	India ink	Teflon	Raman tomography	830	Bone/ System evaluation

(Continued)

Table 1. (Continued)

AUTHORS	PHANTOM TYPE	MATRIX/ CONTAINER	SCATTERER	ABSORBER	PROBING	RS MODALITY	WAVELENGTH (NM)	SIMULATED TISSUE/ PURPOSE OF THE STUDY
Esmonde-White et al,[46] Demers et al[48]	Hydrogel	Gelatin	Liposyn	–	HAP	Raman tomography	785	Bone/ System evaluation for transcutaneous imaging
Esmonde-White et al[50]	Hydrogel	Gelatin	Liposyn II	–	HAP	Raman fiber optic probe	785	Bone / Proof-of-principle for arthroscopic measurements
					CS			Cartilage / Proof-of-principle for arthroscopic measurements
Masson et al[124]	Hydrogel	Gelatin	–	–	Water	Fiber optic RS	680, 785	Cervix/ Water content assessment during pregnancy
Okagbare et al[47,51,52]	Hydrogel	Gelatin	Intralipid	Hb	HAP	Raman fiber optic probe	830	Bone/ System evaluation for transcutaneous measurements
Okagbare and Morris[53]						FEP Raman probe		Bone/ System evaluation
Patil et al[125]	Hydrogel	Gelatin	PS microsphere	–	Naphthalene, BMSB	OCT-guided Raman spectroscopy	785	System evaluation
Meinhardt-Wollweber et al[126]	Hydrogel	Suprasil cuvettes	PVA hydrogel	β-carotene	β-carotene	Resonance RS	440-534	Design evaluation of a multimodal phantom
Bergholt et al[127]	Hydrogel	Type-B gelatin	Induced fiber probe background		–	Fiber optic RS	785	Evaluation of fiber probe background as internal standard
Chaiken et al[80]	Hydrogel	Gelatin	Bovine erythrocytes, Hb (fluorescence)		Glucose	Tissue modulated RS	785	System evaluation for the detection of glucose in blood
Liu et al[68]	Hydrogel	Agarose	Urea and potassium formate with and without PS microspheres		Ratio of 2 layers	Depth sensitive RS	785	Human dermis and epidermis/ System evaluation
Keren et al[128]	Hydrogel	Agarose	Lipid	India ink	SWNTs/ SERS NPs	Raman microspectroscopy	785	Evaluation of maximum penetration depth
Bohndiek et al[129]	Hydrogel	Agarose	Liposyn II	Agarose	S440 SERS NPs	Raman ''imaging''	785	Evaluation of maximum penetration depth
Rodrigues et al[130]	Hydrogel	Bacteriological agar	Chicken egg albumen	NaphtholGreen dye	–	Conventional RS	785	Assessment of thermal coagulation in phantoms
Liu et al[96]	Hydrogel	Agarose	–	–	Gold nanostars (SERS NPs) on breast cancer cells	SERS	850	Evaluation of Quintuple-modality nanoprobe
Odion et al[100-103]	Hydrogel	Agarose gel in a skull	Latex microspheres	Hb	Nanostars (SERS NPs)	Inverse SORS	785	Brain/ Evaluation of SESORS for brain cancer detection
Moody et al[131]	Hydrogel	Agarose gel in a skull	–	–	Gold SERS NPs	SESORS	785	Brain/ Detection of neurotransmitters
Nicolson et al[57]	Hydrogel	Agarose	Fixed mouse skull wrapped in porcine tissue		PTFE	SORS	785	Brain/ Evaluation of SESORS for brain tumor detection

(Continued)

Table 1. (Continued)

AUTHORS	PHANTOM TYPE	MATRIX/ CONTAINER	SCATTERER	ABSORBER	PROBING	RS MODALITY	WAVELENGTH (NM)	SIMULATED TISSUE/ PURPOSE OF THE STUDY
Kircher et al[98]	Hydrogel	Agarose	Liposyn	India ink	MPR NPs	Confocal RS	785	System evaluation for detection threshold and depth of penetration in surgical margins
Qiu et al[99]	Hydrogel	Agarose	Liposyn	–	GERTs SERS NPs	Confocal RS	785	Evaluation of NPs' photothermal depth
Yuen and Liu[92,93]	Hydrogel	Agarose	Intralipid	Nigrosin	Rhodamine 6G, glucose	Confocal RS (SERS)	785	Skin/ Evaluation of Ag microneedle for intradermal glucose detection
Gao et al[69]	Hydrogel	Agarose	Intralipid	Nigrosin	*Trans*-stilbene	Photoacoustic-guided depth-resolved RS	785	Skin/ System evaluation for depth localization
Reble et al[72,73]	Solid	Silicone	TiO_2	Red silopren	β-carotene	Raman and spatially resolved reflectance spectroscopy	488	Skin/ Raman signal correction
Iping Petterson et al[132]	Solid	PDMS	TiO_2	–	$CaCO_3$, HAP	Time-Resolved RS, SORS and combinations	720	System comparison
Mosca et al[67]	Solid	–	PE		Paracetamol	SORS + TRS based on differential transmittance	830	Breast/ Depth prediction of lesion
Roig et al[70]	Solid	PDMS	TiO_2		–	Confocal RS	532	Skin/ Correction of in-depth Raman signal
Roig et al[71]			TiO_2	Blue dye/ black ink	PDMS			
Tuchin et al[81]	Solid	Epoxy resin	TiO_2	Red ink	7 layers	Confocal RS	785	Fingernail/ System evaluation
Sekar et al[133]	Solid	PDMS	TiO_2	Printer ink (cyan)	Calcite	Frequency Offset RS (FORS)	700, 745, 780, 808	System evaluation
Dooley et al[56]	Solid	PCL/ DCM	–	–	HAP	SORS (DMD)	785	Bone/ Evaluation of SORS for monitoring tissue mineralization
Maher et al[134]	Liquid	Glass substrates	Intralipid	–	Caffeine powder	Coded aperture RS	785	Assessment of tissue performance for in-depth measurements
	Animal		Chicken breast, porcine buccal tissue					
Srinivasan et al[135]	Hydrogel	Agarose	Intralipid	–	Teflon	Image guided- Raman probe	785	System calibration
	Animal	–	Canine tibia		Bone			System evaluation
Schulmerich et al[45]	Hydrogel	agar	Intralipid	–	Teflon	Raman tomography	785	Bone/ CT data calibration
	Animal	Canine tibia	–	–	–			
Khan et al[136]	Solid	Petri dish	Acetaminophen and paraffin		Ratio of 2 layers	RS- OCT	785	System evaluation for in-depth measurements
	Animal	–	Epithelial and stromal tissue from goat mucus					

(Continued)

Table 1. (Continued)

AUTHORS	PHANTOM TYPE	MATRIX/ CONTAINER	SCATTERER ABSORBER	PROBING	RS MODALITY	WAVELENGTH (NM)	SIMULATED TISSUE/ PURPOSE OF THE STUDY
Khan et al[137]	Solid	–	Acetaminophen and paraffin	Ratio of 2 layers	Cone-Shell RS	785	System performance evaluation
	Animal		Muscle tissue and Chicken tibia				
Stone and Matousek[60]	Animal	–	Porcine tissue	$Ca_{10}(PO_4)_6(OH)_2$ $CaC2O4{\cdot}(H2O)x$	Transmission RS	830	Breast/Technique evaluation for detection of calcifications
Kerssens et al[43]							
Baker et al[65]	Animal	Fused silica slides	Chicken breast	HAP, COHAP and COD	picosecond Kerr-gated RS	490	Breast/ Technique evaluation for detection of calcifications
Stone et al[64]	Animal	–	Chicken breast and skin	HAP, COHAP, COM	SORS	830	Breast/ System evaluation for detection of calcifications
Ghita et al[59]	Animal	–	Porcine tissue	*Trans*-stilbene	TRS	770-830	Breast/ System optimization for detection of calcifications
Ghita et al[61,62]				HAP and/or PTFE		808	
Mo et al,[138] Wang et al[139]	Animal	–	Chicken muscle and fat tissue	2-layer ratio	Ball lens Raman probe	785	Epithelial tissue/ System performance evaluation
					Raman endoscopic probe		
Stone et al[110]	Animal	–	Porcine muscle tissue	SERRS-active NPs (Agc)	SERRS combined with TRS	830	Dense human tissue/ System evaluation for tumor detection
Stone et al[107]	Animal	–	Porcine tissue	SERS NPs	Multiplexed SESORS imaging	830	Dense human tissue/ Evaluation of recovery Raman signal
Mosca et al[106]	Animal	–	Porcine tissue	Gold NPs	SERS combined with SORS + TRS	830	System evaluation of inclusion detection and depth prediction
Xie et al[109]	Animal	–	Porcine muscle tissue	SERS NPs + bisphosphonates	SESORS	830	Feasibility demonstration of bone-specific NPs detection below tissue
Dey et al[105]	Animal	–	Chicken breast tissue	Gold SERS NPs	SESORS	785	System evaluation
Asiala et al[104]	Animal	Glass slides	Porcine tissue	SERS NPs	SESORS	785	System evaluation
Sharma et al[140]	Animal	–	Ovine tissue attached to bone	BPE SERS nanotags	SESORS	785	Proof-of-concept/ Acquisition of signal through the bone
Wang et al[108]	Animal	–	Lean pork tissue	Gold SERS NPs in gelatin	SORS and Raman tomography in a reflectance mode	785	System evaluation

Abbreviations: BMSB, 1,4-bis(2-methylstyryl)-benzene; BPE, trans-1,2-bis(4-pyridyl)-ethylene; COD, calcium oxalate (dihydrate); COHAP, carbonate substituted hydroxyapatite; COM, calcium oxalate monohydrate; CS, chondroitin sulfate; DCM, dichloromethane; DMD, digital micro-mirror device; FEP, fluorinated ethylene-propylene copolymer; FORS, frequency offset Raman spectroscopy; HAP, hydroxyapatite; Hb, hemoglobin; MPR, magnetic resonance imaging–Photoacoustic imaging–Raman imaging; OCT, optical coherence tomography; PCL, polycaprolactone; PDMS, polydimethylsiloxane; PE, polyethylene; PET, polyethylene terephthalate; PS, polystyrene; PTFE, polytetrafluoroethylene; PVA, polyvinyl alcohol; RS, Raman spectroscopy; SERS, surface-enhanced Raman spectroscopy; SERRS, surface-enhanced resonance Raman scattering; SESORS, surface-enhanced spatially offset Raman spectroscopy; SORS, spatially-offset RS; SWNTs, single walled carbon nanotubes; TRS, transmission RS.

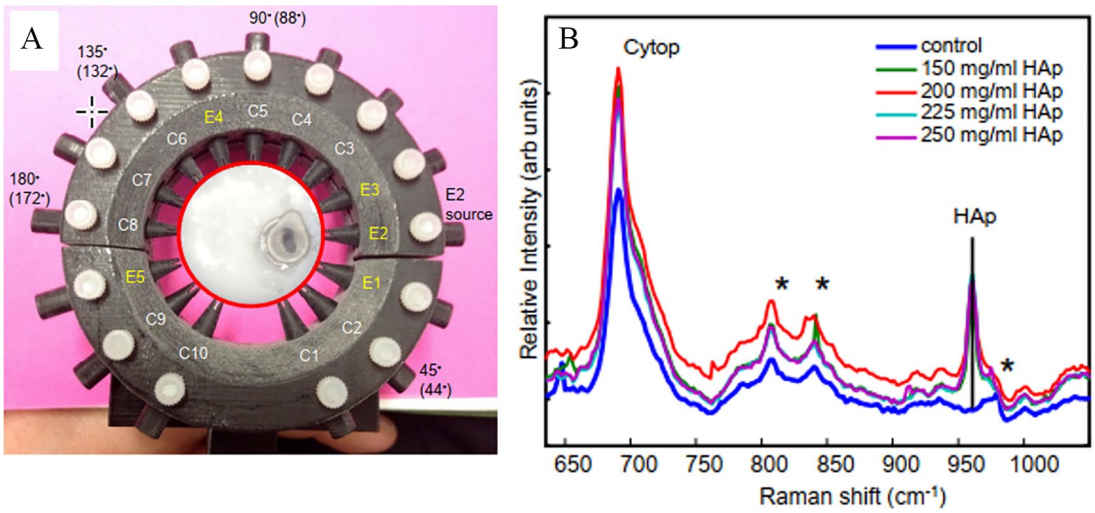

Figure 4. (A) Photograph of a tissue phantom with a mineral "bone" inclusion (HAP) embedded in the centrifuge material (Cytop) and placed in the fiber holder of a Raman tomographic imaging setup. (B) Raman signal acquired with the collection fibers, for different HAP concentrations of the "bone" phantom inside its plastic centrifuge tube.
Source: Adapted with permission from Demers et al[48] © The Optical Society.

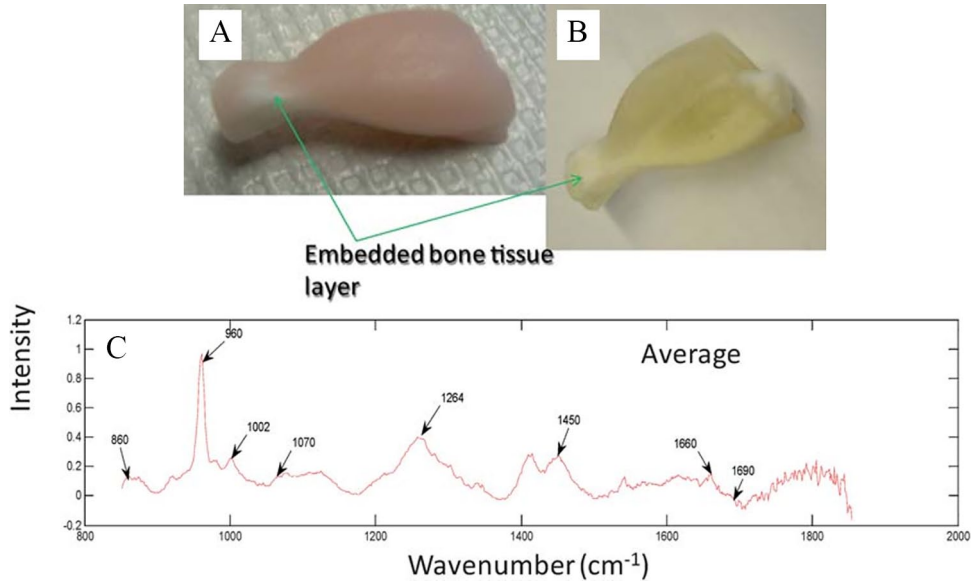

Figure 5. (A) Rat tissue phantom reconstructed from a rat leg model. (B) Rat tissue phantom reconstructed as in (A) but with hemoglobin and Intralipid omitted to make the bone layer visible. (C) Rat tissue phantom transcutaneous Raman spectrum of the bone layer showing major Raman bands (average signal recovered from 47 individual collection fibers).[47]

Liquid and solid tissue phantoms both lack realistic complexity that can be otherwise found in mammalian tissue. To further improve the realistic complexity of such phantoms, multiple layers of identical or different optical parameters and Raman-scattering features have been introduced to the bulk matrix. An example of the latter is well-represented by mineral inclusions, commonly used to enhance the biological importance of phantoms simulating rich-calcification tissues (eg, breast). Inclusions of hydroxyapatite (HAP), a type of apatite synthesized calcification powder, are often added inside the phantom to represent pathological calcifications.[43] Other strong scattering materials, such as calcium carbonate, *trans*-stilbene or polymers, can also be used, especially when there is a need of multiple inclusions with different scattering and distribution within the simulated tissue. Liquid tissue phantoms allow for easy addition or removal of inclusion in the sample volume. In contrary, robust phantoms cannot easily incorporate inclusion features following fabrication, but allow for the presence of a more realistic surrounding tissue such as in the case of animal phantoms.

Tissue Phantoms in Biomedical Applications

Optical tissue phantoms have a wide and diverse range of biomedical applications in the field of Raman spectroscopy (Table 1), and especially deep RS and Raman fiber probe measurements, where the studies mainly focus around lesion detection in cancer and bone disease diagnosis, or glucose sensing in blood. Numerous applications of tissue phantoms can be also found in

the field of surface-enhanced Raman spectroscopy (SERS), where the signal of the molecule of interest can be significantly enhanced using nanoparticles. This review outlines most of the aforementioned applications, with an emphasis on the types of phantoms employed in each case.

Bone studies

Optical phantoms of osteochondral tissues are regularly used to simulate Raman measurements on either bone or soft tissue. Such phantoms are employed for the study of bone diseases or system optimization and characterization. In these studies, by probing the bone below soft tissue, Raman spectroscopy can provide useful information on (a) bone demineralization relevant to osteoporosis or other metabolic bone diseases, and (b) bone changes induced by rheumatoid arthritis or monitoring of bone graft osseointegration.

Raman tomography is a modality providing Raman signal combined with spatial and distribution information of the sample. The setup arrangements either consist of multiple excitation and collection fibers surrounding the sample, or by acquiring signal of a rotating sample in a transmission mode. Tissue phantoms have been employed in both modalities to assist the recovery of Raman signals from subsurface bone tissue. Schulmerich et al acquired computed tomographic (CT) data from skin and bone animal tissue. The CT data were then calibrated against scattering phantoms of agarose matrix with a Teflon sphere inclusion, in order to reconstruct a canine limb through diffuse Raman tomography.[44,45] Apart from calibration reasons, bone tissue phantoms have also been employed for optimization and system development in Raman tomography. In a fiber optic coupled Raman system for measurements on musculoskeletal tissues, gelatin tissue phantoms with a mineral inclusion have been used for the optimization of the position of excitation and collection fibers.[46,47] Esmonde-White et al[46] have measured phantoms of human lower and upper extremities with a variety of fiber optic probe configurations for specific anatomical sampling locations. It was shown that although the transcutaneous Raman signal of the bone could be recovered from 1 to 3 cm of soft tissue, the signal significantly depends on the phantom and therefore the anatomical location geometry. A follow-up study confirmed the feasibility of transcutaneous bone Raman measurements using Raman tomographic imaging, by testing tissue phantoms with mineral inclusions in the range of physiological HAP concentration in bone (Figure 4).[48] The system response was assessed through the contrast between the mineral and background (surrounding tissue) signal, whereas a multichannel detection version of the technique demonstrated multifold sensitivity and highly accurate position recovery of the inclusion.[49]

A different simulation of osteochondral interfaces has been achieved with scattering gelatin-based phantoms consisted of HAP and chondroitin sulfate to mimic bone and cartilage, respectively. Measurements on tissue phantoms of different optical properties which were conducted using fiber-optic Raman spectroscopy,[50] indicated that osteoarthritis parameters, such as optical scattering and thickness of cartilage, significantly affect photon propagation in the tissue and the subsequent bone signal recovery.

In other Raman fiber optic studies, rat tissue phantoms have acted as the intermediate stage for assessing the quality of implanted grafts.[51-53] The gelatin-based phantoms were constructed in line with CT scans and in identical morphology to a rat leg (Figure 5). The phantoms incorporated scattering (Intralipid), absorption (Hemoglobin), and fluorescence (Hemoglobin and Hydroxyapatite) properties, which allowed calibration of the system's response (position of the fibers) for the assessment of bone quality during graft osseointegration.[47]

Deep Raman spectroscopy, an emerging field of RS mainly consisting of spatially offset RS (SORS) and transmission RS (TRS), has utilized tissue phantoms to demonstrate feasibility of acquiring Raman signals from different sampling depths. The technology is based on decoupling the excitation from the collection area and has been extensively applied in the biomedical field.[54,55] In the case of applications related to bone, SORS has been employed to non-invasively assess the mineralization of bone underneath skin, in tissue engineering scaffolds implanted in a sheep bone defect. Dooley et al[56] conducted measurements on 3D printed composite scaffolds with polycaprolactone (PCL) and hydroxyapatite (HA) microparticles, for which the concentration of HA varied to simulate different degrees of mineralization. The study demonstrated feasibility of the approach and a promising monitoring tool for bone healing. Last, tissue phantoms have also been used for the optimization of SORS setups, such as in the case of a mice skull which was wrapped in porcine tissue and filled with agarose gel and a polytetrafluoroethylene (PTFE) sheet inside.[57] The measurements were analyzed to assess the optimum spatial offset for the detection of the PTFE inclusion within the skull.

Breast cancer studies

Raman spectroscopy has been extensively applied to breast cancer diagnostics as an analytical tool. Its application has been reinforced by the presence of breast calcifications, small calcium deposits in human breast which can be benign or related to cancer. Their chemical composition varies and can be either calcium oxalate (type I) or calcium phosphate (type II), mainly hydroxyapatite.[58] Due to their high clinical significance, detection of calcifications has given rise to the employment of breast tissue phantoms in Raman spectroscopy, with calcification-like inclusions of a high Raman cross-section compound (hydroxyapatite, *trans*-stilbene, etc) to represent a malignant element in the phantom matrix.

In transmission Raman measurements conducted by Kerssens et al,[43] the phantom inclusions consisted of various concentrations of either calcium oxalate or calcium phosphate (standing for type I and type II calcifications, respectively) contained in

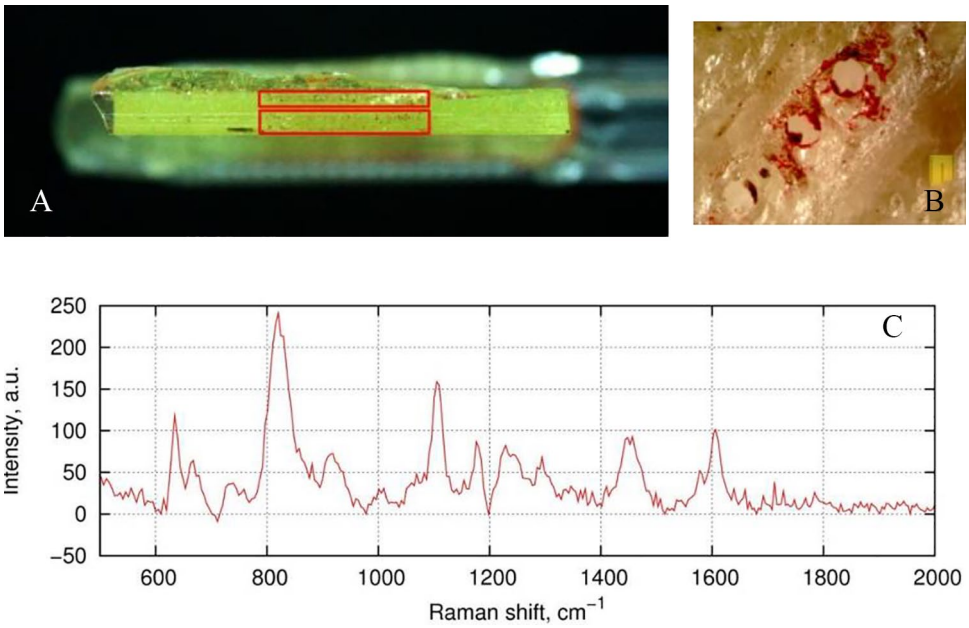

Figure 6. (A) The side view of a fingernail tissue phantom with capillaries. Red lines show upper and lower layer (75 capillaries per layer) of the designed capillary system. (B) Magnified image of the tissue phantom (three holes after red ink testing). (C) Raman spectrum of the tissue phantom basic material (epoxy resin).[81]

quartz cuvettes which were in turn buried in porcine tissue. In a follow-up study, the selection of the optimum excitation wavelength for the optimization of the setup was achieved through TRS measurements on animal phantoms with inclusions of higher Raman cross-section, such as *trans*-stilbene.[59] The animal tissue chosen in such studies was porcine shoulder tissue, due to its composition of mixed fat and protein, similar to that of human breast.[43,60-62] In further deep Raman studies, researchers employed liquid tissue phantoms of Intralipid solution and India ink, adjusting their optical properties to match those of the calcification-rich tissues of breast and prostate.[19,42,63] The origin of the Raman signal of the calcification-like inclusion within the phantom volume was studied as a function of the phantom optical properties in a transmission mode, with the aim to inform future design of Raman probes for cancer diagnosis.

Phantoms of chicken and human breast tissue with calcification-material inclusions were employed in different modes of RS, such as spatially offset Raman spectroscopy[64] and picosecond Kerr-gated,[65] respectively, in order to assess the feasibility of calcification detection within the tissue. It is worth mentioning recent efforts that have been made with liquid and solid phantoms using combined sample differential transmittance (ie, differential attenuation of Raman photons at different wavelengths due to optical properties) and deep Raman spectroscopy, toward the non-invasive prediction of the depth of inclusions representing cancer lesions within turbid matrices.[66,67]

Skin studies

Various skin optical phantoms have been employed for calibration of Raman spectroscopic systems for potential skin cancer detection. Liu et al fabricated an agarose two-layer phantom with scattering similar to dermis and epidermis, introducing polystyrene microspheres in the matrix. Each phantom layer contained either urea or potassium formate as a Raman scatterer. The Raman signal ratio of the two was assessed to evaluate the performance of a snapshot depth sensitive Raman system. The system was evaluated on the basis of its ability to acquire signals from different depths of tissue phantoms, as well as ex vivo animal and in vivo human (fingernail) tissue.[68] Multimodality skin tissue phantoms have also been employed in studies to demonstrate the effectiveness of combined system approaches, such as in the case of a photo-acoustic Raman probe.[69] The multi-layer agarose phantom employed in the study, contained Intralipid and nigrosin dye to simulate skin tissue with a malignant tumor, represented by a *trans*-stilbene inclusion. All of the studies have yielded positive results on potential depth localization of skin tumors and assessment of cancer margins, paving the way for future skin cancer diagnostics.

In the field of skin diagnostics, phantoms have been used for system calibration to correct Raman signal in terms of both optical properties (spectral distorting from elastic scattering) and sample depth. For the correction of in-depth Raman signals in confocal Raman spectroscopy, Roig et al fabricated polydimethylsiloxane (PDMS) scattering skin phantoms of known optical properties with[70] and without absorption.[71] In the latter and more realistic approach, the measurements allowed for signal correction on skin phantoms consisting of multiple layers, each one of them representing a different skin layer (dermis, epidermis, stratum corneum) with distinct optical properties. Other studies including resonance Raman measurements on silicone skin phantoms combined with Monte Carlo simulations[72] have suggested correction functions for the Raman signal of carotenoids (a main

contributor in skin absorption) in skin, without a priori knowledge of the tissue optical properties.[73]

Blood studies

The non-invasive measurement of blood glucose has become a subject of continuous research in the field of bioanalytics. Tissue phantoms have significantly supported the research development toward that direction. Research groups under M. Feld, R. Dasari, and later I. Barman have employed liquid tissue phantoms of different optical properties and varying glucose concentration in Raman measurements. Importantly, their research was focused on correcting the acquired glucose Raman signal in terms of contribution due to skin optical properties, which were in turn simulated through the tissue phantoms. More specifically, Dingari et al[74] used tissue phantoms to establish that varying optical properties heavily affect the prediction accuracy of blood glucose detection in sample-to-sample variability. In a follow-up study, the researchers employed phantoms with different glucose concentrations to initially calibrate and then demonstrate that Turbidity-Corrected Raman Spectroscopy (TCRS) combined with least-squares analysis[75] or Support Vector Machines (SVM)[76] is able to recover useful spectral information by correcting the signal for intensity and shape distortions due to optical properties' effects. Previous studies by the same research group, utilizing intrinsic Raman spectroscopy, also focused on correcting turbidity-induced variations (ie, spectral variations caused by absorption and scattering), however with the prerequisite of already known diffuse scattering coefficient in the employed phantoms.[77] Datasets from the same study were later used in the application of wavelength selection for linear partial least squares (PLS) and nonlinear calibration support vector regression (SVR), with the latter to exhibit the best predictive accuracy for transcutaneous blood glucose detection.[78] Addressing the spectral variations due to photo-bleaching in blood measurements where autofluorescence is usually encountered, Barman et al[79] have employed shifted subtracted Raman spectroscopy combined with partial least squares to increase the prediction accuracy of glucose detection in liquid phantoms, where the fluorescence has been previously induced with indocyanine green.

In a different study, Chaiken et al have used gelatin phantoms containing bovine erythrocytes and hemoglobin as a fluorescence agent, highlighting that interpatient blood qualities such as hematocrit and microcirculation may introduce higher variability in Raman measurements compared with glucose levels. The Raman spectrometer was calibrated using the employed phantoms for non-invasive *in vivo* measurements of blood glucose in a human fingertip.[80] Also for calibration reasons, epoxy resin solid phantoms have been fabricated using TiO_2 and red ink as a scatterer and an absorber, respectively.[81] The researchers of the study achieved to design phantoms exhibiting not only optical properties similar to those of human fingernail, but also simulating the underlying skin tissue with several different layers including glass capillaries filled with red ink (blood) (Figure 6).

In the category of blood equivalent tissue phantoms, it is worth mentioning the case of washed red blood cells suspended in saline instead of plasma[82] and matched in optical properties to human blood.[83] Rather than assess or optimize an instrument performance, those phantoms serve to eliminate interpatient variability during measurements, as plasma carries most of the blood chemical variability.

SERS applications

SERS is a modified Raman technique where the sample is being absorbed onto a nano-colloidal metallic surface (typically silver or gold).[84] Due to the surface plasmon resonance of the metallic nanostructures, Raman signals of specific molecules can be amplified, leading to increased detection sensitivity of the analyte.

Numerous studies have included the simplest type of liquid tissue phantoms, in order to determine the depth of detection of the nanoparticles (NPs) for different Raman imaging systems. The approach consisted of Raman measurements from a capillary or Tygon tube with NPs immersed in varying depth of a scattering agent (ie, Intralipid).[85-87]

Hydrogel tissue phantoms made of Matrigel, polyvinyl alcohol (PVA), and agarose also play a significant part in SERS measurements for biomedical applications. Matrigel tumor phantoms stained with nanoparticles have been employed to demonstrate feasibility of imaging on a rat esophagus with a Raman endoscope.[88] Moran et al used PVA phantoms to study the effect of NPs aggregation on the SERS signal intensity. The NPs Raman signal has been shown to increase with NPs aggregation.[89] It is worth mentioning here that although not commonly used, PVA gels are able to match in optical properties soft tissues, by undergoing freezing and thawing cycles.[90]

Among hydrogel phantoms, the agarose-based are the most commonly employed ones in several SERS studies, for example in assessing the repeatability and stability of a SERS sensor array for pH measurements.[91] In the field of non-invasive blood glucose monitoring, researchers have used them to demonstrate proof-of-concept SERS measurements using an Ag-coated microneedle.[92,93] The agarose skin-mimicking phantoms were enhanced with Intralipid and nigrosin to mimic human skin. The approach was later employed in combination with resonance enhancement, to detect malaria in blood.[94] Chenet al[95] have composed an excellent review on the applications of SERS through skin. Other SERS applications include employment of tumor phantoms (breast cancer cells in agarose medium) for the development of a plasmonic nanoprobe utilized for in vivo photothermal therapy in tumors.[96]Agarose tissue phantoms have been used for NP-assisted cancer tissue scanning (ie, surgical margins), more specifically to assess the NP detection

threshold,[97] the depth of penetration,[98] and their photothermal effect.[99] To better simulate the optical properties of the tissue, scattering (Liposyn) and/or absorbing (India ink) agents were added in the phantoms of the last two studies.

The combination of SERS and SORS (SESORS) has quickly led to the most clinically relevant applications, as it allows for non-invasive and highly sensitive probing of nanoparticle-conjugated biomolecules in different sampling depths. Both tissue and animal phantoms have been employed in SESORS measurements, especially in studies focused on brain tumor detection. Gel phantoms made of an agarose matrix with optical properties equivalent to brain tissue and infused with NPs were contained in a skull to demonstrate feasibility of the SESORS approach in brain cancer.[100-103]

On their end, animal tissue phantoms in SERS studies have served as models for the evaluation of the maximum penetration depth in tissues through which a distinct signal from the SERS-active NPs could be obtained. In those studies, one must consider the multiple parameters affecting the assessment of penetration depth using nanoparticles, such as concentration and degree of conjugation achieved. With a combination of SERS and deep Raman spectroscopy (SORS and transmission),[104,105] researchers have used NPs to probe a localized inclusion (ie, cancer lesion) in animal tissues and evaluate the NP maximum penetration depth. A recent application of combined SERS, SORS and transmission Raman in porcine tissue, has yielded high accuracy not only in terms of NPs' signal detection but also of their depth prediction.[106] Other applications of combined SERS and deep Raman spectroscopy in porcine tissue phantoms include multiplexed imaging,[107] combined Raman tomography,[108] and drug detection.[109] Stone et al[110] have specifically combined transmission RS with SERS to improve the detection limit of resonance (SERRS) active nanoparticles in animal tissue, leading toward the prospect of small tumor identification. Nicolson et al[57] used plasmon resonance active nanoparticles, leading to the first in vivo application of SESORRS (Surface-Enhanced Spatially Offset Resonance Raman Spectroscopy) for the detection of brain tumor in rats after the SORS signal has been optimized in equivalent agarose tissue phantoms.

Last, it is worth mentioning a multimodal approach of combined photoacoustic and Raman imaging, where Shi et al[111,112] employed a special case of phantoms to evaluate SERS imaging for the detection of breast cancer cells tagged with NPs. The cells targetted with nanoparticles were suspended in rat blood flowing within an acrylic capillary tube, achieving in that way a more realistic blood microvasculature imaging (Table 1).

Closing Remarks

There is a large number of optical tissue phantoms covering a wide range of shapes, geometries, and optical properties. Due to their flexibility in design, time-efficiency and low-cost fabrication, optical tissue phantoms are now a standard part of instrumentation for studies translating into a clinical environment. However, even if their geometry mimics the tissue of interest accurately, the phantoms are only able to simulate the absorption and scattering of the tissue on a large scale. Their composition and lack of heterogeneity do not allow for accurate representation of the complicated optical properties arising from cellular and subcellular features within the tissue. For that reason, although tissue phantoms are an indispensable part of research development and validation, ex vivo tissue has also been introduced in their place.

Advances on tissue engineering and 3D printing hold great promise for further development of tissue phantom technology. The rapidly evolving field of 3D printing can support increasing refinement of the phantom composition, contributing to a more realistic structure. Although 3D phantoms in Raman Spectroscopy are not very common, an excellent review of their qualities and limitations in other imaging techniques has been composed by Filippou and Tsoumpas.[141]

Together with ex vivo tissue, tissue engineering can become an established alternative to the standard tissue phantoms, serving the needs of current technology and applications. One of these challenges consists of the employment of multiple approaches within the same study. Optical and spectroscopic techniques are constantly combined with standard clinical imaging (magnetic resonance imaging, X-rays, optical coherence tomography) to further advance biomedical research. As part of this development, the efficiency in cost and time is pushing toward the fabrication of multimodality phantoms. Although this is a desirable concept, it is also highly challenging as different techniques require different properties integrated into the phantoms.

Further research is required to take full advantage of tissue phantoms as a useful tool not only for the better understanding of biological systems, but also for the more efficient development of diagnostic and therapeutic approaches.

Author Contributions

MV and NK outlined the scope of the review, and MV developed the initial manuscript draft. All authors participated in developing the final manuscript.

ORCID iDs

Martha Z Vardaki https://orcid.org/0000-0002-9624-8363
Nikolaos Kourkoumelis https://orcid.org/0000-0003-3264-2406

Supplemental Material

Supplemental material for this article is available online.

REFERENCES

1. Auner GW, Koya SK, Huang C, et al. Applications of Raman spectroscopy in cancer diagnosis. *Cancer Metastasis Rev*. 2018;37:691-717.
2. Neugebauer U, Rosch P, Popp J. Raman spectroscopy towards clinical application: drug monitoring and pathogen identification. *Int J Antimicrob Agents*. 2015;46:S35-S39.

3. Kourkoumelis N, Gaitanis G, Velegraki A, Bassukas ID. Nail Raman spectroscopy: a promising method for the diagnosis of onychomycosis. An ex vivo pilot study. *Med Mycol*. 2018;56:551-558.
4. Muro CK, Doty KC, Fernandes LD, Lednev IK. Forensic body fluid identification and differentiation by Raman spectroscopy. *Forensic Chem*. 2016;1:31-38.
5. Vardaki MZ, Atkins CG, Schulze HG, et al. Raman spectroscopy of stored red blood cell concentrate within sealed transfusion blood bags. *Analyst*. 2018;143:6006-6013.
6. Devitt G, Howard K, Mudher A, Mahajan S. Raman spectroscopy: an emerging tool in neurodegenerative disease research and diagnosis. *ACS Chem Neurosci*. 2018;9:404-420.
7. Petrokilidou C, Gaitanis G, Bassukas ID, et al. Emerging optical techniques for the diagnosis of onychomycosis. *Appl Sci*. 2020;10:2340.
8. Pavlou E, Zhang XZ, Wang J, Kourkoumelis N. Raman spectroscopy for the assessment of osteoarthritis. *Ann Jt*. 2018;3:83.
9. Huong PV. Drug analysis by Raman and micro-Raman spectroscopy. *J Pharm Biomed Anal*. 1986;4:811-823.
10. Rangan S, Schulze HG, Vardaki MZ, Blades MW, Piret JM, Turner RFB. Applications of Raman spectroscopy in the development of cell therapies: state of the art and future perspectives. *Analyst*. 2020;145:2070-2105.
11. Cerussi AE, Warren R, Hill B, et al. Tissue phantoms in multicenter clinical trials for diffuse optical technologies. *Biomed Opt Express*. 2012;3:966-971.
12. Pogue BW, Patterson MS. Review of tissue simulating phantoms for optical spectroscopy, imaging and dosimetry. *J Biomed Opt*. 2006;11:041102.
13. Tuchin VV. *Tissue Optics, Light Scattering Methods and Instruments for Medical Diagnosis*. 2nd ed. Bellingham, WA: Society of Photo-Optical Instrumentation Engineers (SPIE); 2015.
14. Esmonde-White FW, Esmonde-White KA, Kole MR, Goldstein SA, Roessler BJ, Morris MD. Biomedical tissue phantoms with controlled geometric and optical properties for Raman spectroscopy and tomography. *Analyst*. 2011;136:4437-4446.
15. Jheng Y-C, Lin C-L. Fabrication and testing of breast tissue-mimicking phantom for needle biopsy cutting: a pilot study. Paper presented at: 2017 Design of Medical Devices Conference; April 10-13, 2017; Minneapolis, MN.
16. In E, Naguib H, Haider M. Mechanical stability analysis of carrageenan-based polymer gel for magnetic resonance imaging liver phantom with lesion particles. *J Med Imaging (Bellingham)*. 2014;1:035502.
17. Arteaga-Marrero N, Villa E, Gonzalez-Fernandez J, Martin Y, Ruiz-Alzola J. Polyvinyl alcohol cryogel phantoms of biological tissues for wideband operation at microwave frequencies. *PLoS ONE*. 2019;14:e0219997.
18. Mosca S, Lanka P, Stone N, et al. Optical characterization of porcine tissues from various organs in the 650–1100 nm range using time-domain diffuse spectroscopy. *Biomed Opt Express*. 2020;11:1697-1706.
19. Vardaki M. *Advanced Raman Techniques for Real Time Cancer Diagnostics* [PhD thesis]. Exeter, UK: Physics, University of Exeter;2016.
20. Jacques SL. Optical properties of biological tissues: a review. *Phys Med Biol*. 2013;58:R37-R61.
21. Arnfield MR, Tulip J, McPhee MS. Optical propagation in tissue with anisotropic scattering. *IEEE Trans Biomed Eng*. 1988;35:372-381.
22. Jacques SL, Alter C, Prahl SA. Angular dependence of HeNe laser light scattering by human dermis. *Lasers Life Sci*. 1987;1:309-333.
23. Yavari N. *Optical Spectroscopy for Tissue Diagnostics and Treatment Control* [doctoral thesis]. Bergen, Norway: University of Bergen;2006.
24. Mourant JR, Freyer JP, Hielscher AH, Eick AA, Shen D, Johnson TM. Mechanisms of light scattering from biological cells relevant to noninvasive optical-tissue diagnostics. *Appl Opt*. 1998;37:3586-3593.
25. Salomatina E, Jiang B, Novak J, Yaroslavsky AN. Optical properties of normal and cancerous human skin in the visible and near-infrared spectral range. *J Biomed Opt*. 2006;11:064026.
26. Bevilacqua F, Piguet D, Marquet P, Gross JD, Tromberg BJ, Depeursinge C. In vivo local determination of tissue optical properties: applications to human brain. *Appl Opt*. 1999;38:4939-4950.
27. O'Sullivan TD, Cerussi AE, Cuccia DJ, Tromberg BJ. Diffuse optical imaging using spatially and temporally modulated light. *J Biomed Opt*. 2012;17:071311.
28. Tromberg BJ, Coquoz O, Fishkin J, et al. Non-invasive measurements of breast tissue optical properties using frequency-domain photon migration. *Philos T R Soc B*. 1997;352:661-668.
29. Bashkatov AN, Genina EA, Kochubey VI, Tuchin VV. Optical properties of human cranial bone in the spectral range from 800 to2000 nm—art. no. 616310. *Proc SPIE*. 2006;6163:16310.
30. Germer CT, Roggan A, Ritz JP, et al. Optical properties of native and coagulated human liver tissue and liver metastases in the near infrared range. *Lasers Surg Med*. 1998;23:194-203.
31. Strömblad S. *Measuring the Optical Properties of Human Muscle Tissue Using Time-of-Flight Spectroscopy in the Near Infrared* [master's thesis]. Lund, Sweden: Lund University; 2015.
32. Bashkatov AN, Genina EA, Kochubey VI, et al. Optical properties of human stomach mucosa in the spectral range from 400 to 2000 nm. Paper presented at: International Conference on Lasers, Applications, and Technologies 2007: Laser Technologies for Medicine; August 1, 2007:6734; Minsk, Belarus.
33. Ao HL, Xing D, Wei HJ, Gu HM, Wu GY, Lu JJ. Thermal coagulation-induced changes of the optical properties of normal and adenomatous human colon tissues in vitro in the spectral range 400-1100 nm. *Phys Med Biol*. 2008;53:2197-2206.
34. Pu Y, Wang WB, Al-Rubaiee M, Gayen SK, Xu M. Determination of optical coefficients and fractal dimensional parameters of cancerous and normal prostate tissues. *Appl Spectrosc*. 2012;66:828-834.
35. Bosschaart N, Edelman GJ, Aalders MCG, van Leeuwen TG, Faber DJ. A literature review and novel theoretical approach on the optical properties of whole blood. *Lasers Med Sci*. 2014;29:453-479.
36. Hung CH, Chou TC, Hsu CK, Tseng SH. Broadband absorption and reduced scattering spectra of in-vivo skin can be noninvasively determined using delta-P-1 approximation based spectral analysis. *Biomed Opt Express*. 2015;6:443-456.
37. Dong EB, Zhao ZH, Wang MJ, et al. Three-dimensional fuse deposition modeling of tissue-simulating phantom for biomedical optical imaging. *J Biomed Opt*. 2015;20:121311.
38. Abildgaard OHA. *Broadband Optical Characterization of Material Properties*. Kongens Lyngby, Denmark:DTU Compute; 2014.
39. Paunescu LA, Michalos A, Choi JH, Wolf U, Wolf M, Gratton E. In vitro correlation between reduced scattering coefficient and hemoglobin concentration of human blood determined by near-infrared spectroscopy. *Proc SPIE*. 2001;4250:319-326.
40. Rossi VM. *Digital Fourier Holographic Microscopy and Potential Applications Towards the Design of Photodynamic Therapy of Osteosarcoma* [PhD thesis].Corvallis, OR: Oregon State University;2015.
41. Michels R, Foschum F, Kienle A. Optical properties of fat emulsions. *Opt Express*. 2008;16:5907-5925.
42. Vardaki MZ, Matousek P, Stone N. Characterisation of signal enhancements achieved when utilizing a photon diode in deep Raman spectroscopy of tissue. *Biomed Opt Express*. 2016;7:2130-2141.
43. Kerssens MM, Matousek P, Rogers K, Stone N. Towards a safe non-invasive method for evaluating the carbonate substitution levels of hydroxyapatite (HAP) in micro-calcifications found in breast tissue. *Analyst*. 2010;135:3156-3161.
44. Schulmerich MV, Cole JH, Dooley KA, et al. Noninvasive Raman tomographic imaging of canine bone tissue. *J Biomed Opt*. 2008;13:020506.
45. Schulmerich MV, Srinivasan S, Kreider J, et al. Raman tomography of tissue phantoms and bone tissue. *Biomed Opt Spectrosc*. 2008;6853:68530V.
46. Esmonde-White FWL, Esmonde-White KA, Morris MD. Exposed and transcutaneous measurement of musculoskeletal tissues using fiber optic coupled Raman spectroscopy. *Proc SPIE*. 2010;7548:75484D.
47. Okagbare PI, Esmonde-White FW, Goldstein SA, Morris MD. Development of non-invasive Raman spectroscopy for in vivo evaluation of bone graft osseointegration in a rat model. *Analyst*. 2010;135:3142-3146.
48. Demers JLH, Esmonde-White FWL, Esmonde-White KA, Morris MD, Pogue BW. Next-generation Raman tomography instrument for non-invasive in vivo bone imaging. *Biomed Opt Express*. 2015;6:793-806.
49. Demers JL, Davis SC, Pogue BW, Morris MD. Multichannel diffuse optical Raman tomography for bone characterization in vivo: a phantom study. *Biomed Opt Express*. 2012;3:2299-2305.
50. Esmonde-White KA, Esmonde-White FW, Morris MD, Roessler BJ. Fiber-optic Raman spectroscopy of joint tissues. *Analyst*. 2011;136:1675-1685.
51. Okagbare PI, Esmonde-White FWL, Goldstein SA, Morris MD. Transcutaneous Raman spectroscopy for assessing progress of bone graft incorporation in bone reconstruction and repair. *Proc SPIE*. 2011;7883:78834I.
52. Okagbare PI, Begun D, Tecklenburg M, Awonusi A, Goldstein SA, Morris MD. Noninvasive Raman spectroscopy of rat tibiae: approach to in vivo assessment of bone quality. *J Biomed Opt*. 2012;17:090502.
53. Okagbare PI, Morris MD. Polymer-capped fiber-optic Raman probe for non-invasive Raman spectroscopy. *Analyst*. 2012;137:77-81.
54. Vardaki MZ, Devine DV, Serrano K, et al. Defocused spatially offset Raman spectroscopy in media of different optical properties for biomedical applications using a commercial spatially offset Raman spectroscopy device. *Appl Spectrosc*.2020;74:223-232.
55. Matousek P, Stone N. Emerging concepts in deep Raman spectroscopy of biological tissue. *Analyst*. 2009;134:1058-1066.
56. Dooley M, Prasopthum A, Liao Z, et al. Spatially-offset Raman spectroscopy for monitoring mineralization of bone tissue engineering scaffolds: feasibility study based on phantom samples. *Biomed Opt Express*. 2019;10:1678-1690.
57. Nicolson F, Andreiuk B, Andreou C, Hsu HT, Rudder S, Kircher MF. Non-invasive in vivo imaging of cancer using surface-enhanced spatially offset Raman spectroscopy (SESORS). *Theranostics*. 2019;9:5899-5913.

58. Busing CM, Keppler U, Menges V. Differences in microcalcification in breast tumors. *Virchows Arch A*. 1981;393:307-313.
59. Ghita A, Matousek P, Stone N. Exploring the effect of laser excitation wavelength on signal recovery with deep tissue transmission Raman spectroscopy. *Analyst*. 2016;141:5738-5746.
60. Stone N, Matousek P. Advanced transmission Raman spectroscopy: a promising tool for breast disease diagnosis. *Cancer Res*. 2008;68:4424-4430.
61. Ghita A, Matousek P, Stone N. High sensitivity non-invasive detection of calcifications deep inside biological tissue using transmission Raman spectroscopy. *J Biophotonics*. 2018;11:e201600260.
62. Ghita A, Matousek P, Stone N. Sensitivity of transmission Raman spectroscopy signals to temperature of biological tissues. *Sci Rep*. 2018;8:8379.
63. Vardaki MZ, Gardner B, Stone N, Matousek P. Studying the distribution of deep Raman spectroscopy signals using liquid tissue phantoms with varying optical properties. *Analyst*. 2015;140:5112-5119.
64. Stone N, Baker R, Rogers K, Parker AW, Matousek P. Subsurface probing of calcifications with spatially offset Raman spectroscopy (SORS): future possibilities for the diagnosis of breast cancer. *Analyst*. 2007;132:899-905.
65. Baker R, Matousek P, Ronayne KL, Parker AW, Rogers K, Stone N. Depth profiling of calcifications in breast tissue using picosecond Kerr-gated Raman spectroscopy. *Analyst*. 2007;132:48-53.
66. Gardner B, Stone N, Matousek P. Noninvasive determination of depth in transmission Raman spectroscopy in turbid media based on sample differential transmittance. *Anal Chem*. 2017;89:9730-9733.
67. Mosca S, Dey P, Tabish TA, Palombo F, Stone N, Matousek P. Spatially offset and transmission Raman spectroscopy for determination of depth of inclusion in turbid matrix. *Anal Chem*. 2019;91:8994-9000.
68. Liu W, Ong YH, Yu XJ, et al. Snapshot depth sensitive Raman spectroscopy in layered tissues. *Opt Express*. 2016;24:28312-28325.
69. Gao F, Ong YH, Li GM, Feng XH, Liu Q, Zheng YJ. Fast photoacoustic-guided depth-resolved Raman spectroscopy: a feasibility study. *Opt Lett*. 2015;40:3568-3571.
70. Roig B, Koenig A, Perraut F, et al. Biophotonics of skin: method for correction of deep Raman spectra distorted by elastic scattering. *Proc SPIE*. 2015;9318: 93180L.
71. Roig B, Koenig A, Perraut F, et al. Multilayered phantoms with tunable optical properties for a better understanding of light/tissue interactions. *Proc SPIE*. 2015;9325:93250B.
72. Reble C, Gersonde I, Helfmann J, Andree S, Illing G. Correction of Raman signals for tissue optical properties. In: Georgakoudi, I, Popp, J, Svanberg, K eds. *Clinical and Biomedical Spectroscopy*. Vol. 7368. Bellingham, WA: Society of Photo-Optical Instrumentation Engineers (SPIE); 2009:7368_0C.
73. Reble C, Gersonde I, Andree S, Eichler HJ, Helfmann J. Quantitative Raman spectroscopy in turbid media. *J Biomed Opt*. 2010;15:037016.
74. Dingari NC, Barman I, Singh GP, Kang JW, Dasari RR, Feld MS. Investigation of the specificity of Raman spectroscopy in non-invasive blood glucose measurements. *Anal Bioanal Chem*. 2011;400:2871-2880.
75. Barman I, Singh GP, Dasari RR, Feld MS. Turbidity-corrected Raman spectroscopy for blood analyte detection. *Anal Chem*. 2009;81:4233-4240.
76. Barman I, Kong CR, Dingari NC, Dasari RR, Feld MS. Development of robust calibration models using support vector machines for spectroscopic monitoring of blood glucose. *Anal Chem*. 2010;82:9719-9726.
77. Bechtel KL, Shih WC, Feld MS. Intrinsic Raman spectroscopy for quantitative biological spectroscopy part II: experimental applications. *Opt Express*. 2008;16:12737-12745.
78. Dingari NC, Barman I, Kang JW, Kong CR, Dasari RR, Feld MS. Wavelength selection-based nonlinear calibration for transcutaneous blood glucose sensing using Raman spectroscopy. *J Biomed Opt*. 2011;16:087009.
79. Barman I, Kong CR, Singh GP, Dasari RR. Effect of photobleaching on calibration model development in biological Raman spectroscopy. *J Biomed Opt*. 2011;16:011004.
80. Chaiken J, Finney WF, Knudson PE, et al. Noninvasive blood analysis by tissue modulated NIR Raman spectroscopy. *Proc SPIE*. 2001;4368:134-145.
81. Tuchin VV, Bashkatov AN, Genina EA, et al. Finger tissue model and blood perfused skin tissue phantom. *Proc SPIE*. 2011;7898:78980Z.
82. Gnyba M, Jedrzejewska-Szczerska M, Wrobel MS. Raman spectroscopic investigation of blood and related materials. *Proc SPIE*.2015;9448:944809.
83. Karpienko K, Gnyba M, Milewska D, Wrobel MS, Jedrzejewska-Szczerska M. Blood equivalent phantom vs whole human blood, a comparative study. *J Innov Opt Heal Sci*. 2016;9:1650012.
84. Stiles PL, Dieringer JA, Shah NC, Van Duyne RR. Surface-enhanced Raman spectroscopy. *Annu Rev Anal Chem*. 2008;1:601-626.
85. McVeigh PZ, Mallia RJ, Veilleux I, Wilson BC. Development of a widefield SERS imaging endoscope. *Proc SPIE*. 2012;8217:821704.
86. McVeigh PZ, Mallia RJ, Veilleux I, Wilson BC. Widefield quantitative multiplex surface enhanced Raman scattering imaging in vivo. *J Biomed Opt*. 2013;18:046011.
87. Shi W, Paproski RJ, Moore R, Zemp R. Detection of circulating tumor cells using targeted surface-enhanced Raman scattering nanoparticles and magnetic enrichment. *J Biomed Opt*. 2014;19:056014.
88. Wang Y, Khan A, Leigh SY, Liu JTC. Rapid multiplexed imaging of cell-surface cancer biomarkers in fresh tissues with targeted SERS nanoparticles. Paper presented at: 2014 International Symposium on Optomechatronic Technologies; November 5-7, 2014:149-152; Seattle, WA.
89. Moran CH, Rycenga M, Xia XH, Cobley CM, Xia YN. Using well-defined Ag nanocubes as substrates to quantify the spatial resolution and penetration depth of surface-enhanced Raman scattering imaging. *Nanotechnology*. 2014;25:014007.
90. Kharine A, Manohar S, Seeton R, et al. Poly(vinyl alcohol) gels for use as tissue phantoms in photoacoustic mammography. *Phys Med Biol*. 2003;48:357-370.
91. Park JE, Yonet-Tanyeri N, Vander Ende E, et al. Plasmonic microneedle arrays for in situ sensing with surface enhanced Raman spectroscopy (SERS). *Nano Lett*. 2019;19:6862-6868.
92. Yuen C, Liu Q. Ag coated microneedle based surface enhanced Raman scattering probe for intradermal measurements. *Proc SPIE*. 2013;8798:87980R.
93. Yuen C, Liu Q. Towards in vivo intradermal surface enhanced Raman scattering (SERS) measurements: silver coated microneedle based SERS probe. *J Biophotonics*. 2014;7:683-689.
94. Liu Q, Yuen C, Chen KR, Ju J, Xiong AL, Preiser P. Surface enhanced Raman spectroscopy for Malaria diagnosis and intradermal measurements. *Proc SPIE*. 2018;10509:1050902.
95. Chen K, Ong Y, Yuen C, Liu Q. Surface-enhanced Raman spectroscopy for intradermal measurements. In: Hamblin, MR, Avci, P, Gupta, GK, eds. *Imaging in Dermatology*. Amsterdam, The Netherlands: Elsevier;2016:141-154.
96. Liu Y, Chang Z, Yuan HK, Fales AM, Vo-Dinh T. Quintuple-modality (SERS-MRI-CT-TPL-PTT) plasmonic nanoprobe for theranostics. *Nanoscale*. 2013;5:12126-12131.
97. D'Hollander A, Mathieu E, Jans H, et al. Development of nanostars as a biocompatible tumor contrast agent: toward in vivo SERS imaging. *Int J Nanomedicine*. 2016;11:3703-3714.
98. Kircher MF, de la, Zerda A, Jokerst JV, et al. A brain tumor molecular imaging strategy using a new triple-modality MRI-photoacoustic-Raman nanoparticle. *Nat Med*. 2012;18:829-834.
99. Qiu YY, Zhang YQ, Li MW, et al. Intraoperative detection and eradication of residual microtumors with gap-enhanced Raman tags. *ACS Nano*. 2018;12:7974-7985.
100. Odion RA, Strobbia P, Crawford BM, Tuan VD. Surface-enhanced spatially offset Raman spectroscopy (SESORS) for subsurface detection of nanostar probes. *Proc SPIE*.2019;11007:110070I.
101. Odion RA, Strobbia P, Crawford BM, Tuan VD. Direct detection of nanostar probes through a monkey skull using inverse surface-enhanced spatially offset Raman spectroscopy (SESORS). *Proc SPIE*.2019;10868:108680B.
102. Odion RA, Strobbia P, Crawford BM, Tuan VD. Inverse surface-enhanced spatially offset Raman spectroscopy (SESORS) through a monkey skull. *J Raman Spectrosc*. 2018;49:1452-1460.
103. Odion R, Strobbia P, Vo-Dinh T. Surface-enhanced spatially offset Raman spectroscopy (SESORS) for biomedical applications. *Proc SPIE*.2018;10484:1048404.
104. Asiala SM, Shand NC, Faulds K, Graham D. Surface-enhanced, spatially offset Raman spectroscopy (SESORS) in tissue analogues. *ACS Appl Mater Interfaces*. 2017;9:25488-25494.
105. Dey P, Olds W, Blakey I, Thurecht KJ, Izake EL, Fredericks PM. SERS-based detection of barcoded gold nanoparticle assemblies from within animal tissue. *J Raman Spectrosc*. 2013;44:1659-1665.
106. Mosca S, Dey P, Tabish TA, Palombo F, Stone N, Matousek P. Determination of inclusion depth in ex vivo animal tissues using surface enhanced deep Raman spectroscopy. *J Biophotonics*. 2020;13:e201960092.
107. Stone N, Kerssens M, Lloyd GR, Faulds K, Graham D, Matousek P. Surface enhanced spatially offset Raman spectroscopic (SESORS) imaging—the next dimension. *Chem Sci*. 2011;2:776-780.
108. Wang ZY, Yang H, Ding H, Lu GJ, Jiang HB, Bi XH. Area-detection fibre-optic system for spatially offset Raman spectroscopy and Raman tomography in reflection mode. *Electron Lett*. 2015;51:1684-1685.
109. Xie HN, Stevenson R, Stone N, Hernandez-Santana A, Faulds K, Graham D. Tracking bisphosphonates through a 20 mm thick porcine tissue by using surface-enhanced spatially offset Raman spectroscopy. *Angew Chem Int Edit*. 2012;51:8509-8511.
110. Stone N, Faulds K, Graham D, Matousek P. Prospects of deep Raman Spectroscopy for noninvasive detection of conjugated surface enhanced resonance Raman scattering nanoparticles buried within 25 mm of mammalian tissue. *Anal Chem*. 2010;82:3969-3973.
111. Shi W, Shao P, Paproski R, Forbrich A, Moore R, Zemp RJ. Multimodality photoacoustic and Raman imaging of magnetically trapped tumor cells. *Proc SPIE*.2014;8943:89431X.
112. Shi W, Paproski RJ, Shao P, Forbrich A, Lewis JD, Zemp RJ. Multimodality Raman and photoacoustic imaging of surface-enhanced-Raman-scattering-targeted tumor cells. *J Biomed Opt*. 2016;21:020503.

113. Chuchuen O, Henderson MH, Sykes C, Kim MS, Kashuba ADM, Katz DF. Quantitative analysis of microbicide concentrations in fluids, gels and tissues using confocal Raman spectroscopy. *PLoS ONE*. 2013;8:e85124.
114. Maher JR, Berger AJ. Determination of ideal offset for spatially offset Raman spectroscopy. *Appl Spectrosc*. 2010;64:61-65.
115. McCain ST, Gehm ME, Wang Y, Pitsianis NP, Brady DJ. Coded aperture Raman spectroscopy for quantitative measurements of ethanol in a tissue phantom. *Appl Spectrosc*. 2006;60:663-671.
116. McCain ST, Gehm ME, Wang Y, Pitsianis NP, Brady DJ. Multimodal multiplex Raman spectroscopy optimized for in vivo chemometrics. *Proc SPIE*.2006;6093:60930P.
117. Motz JT, Hunter M, Galindo LH, et al. Optical fiber probe for biomedical Raman spectroscopy. *Appl Opt*. 2004;43:542-554.
118. Maher JR, Chuchuen O, Henderson MH, et al. Co-localized confocal Raman spectroscopy and optical coherence tomography (CRS-OCT) for depth-resolved analyte detection in tissue. *Biomed Opt Express*. 2015;6:2022-2035.
119. Iping Petterson IE, Day JC, Fullwood LM, Gardner B, Stone N. Characterisation of a fibre optic Raman probe within a hypodermic needle. *Anal Bioanal Chem*. 2015;407:8311-8320.
120. Zavaleta C, de la Zerda A, Liu Z, et al. Noninvasive Raman spectroscopy in living mice for evaluation of tumor targeting with carbon nanotubes. *Nano Lett*. 2008;8:2800-2805.
121. Zavaleta CL, Garai E, Liu JTC, et al. A Raman-based endoscopic strategy for multiplexed molecular imaging. *Proc Natl Acad Sci USA*. 2013;110:10062-10063.
122. Brenan CJH, Hunter IW. Volumetric Raman microscopy through a turbid medium. *J Raman Spectrosc*. 1996;27:561-570.
123. Agenant M, Grimbergen M, Draga R, Marple E, Bosch R, van Swol C. Clinical superficial Raman probe aimed for epithelial tumor detection: phantom model results. *Biomed Opt Express*. 2014;5:1203-1216.
124. Masson LE, O'Brien CM, Pence IJ, et al. Dual excitation wavelength system for combined fingerprint and high wave number Raman spectroscopy. *Analyst*. 2018;143:6049-6060.
125. Patil CA, Bosschaart N, Keller MD, van Leeuwen TG, Mahadevan-Jansen A. Combined Raman spectroscopy and optical coherence tomography device for tissue characterization. *Opt Lett*. 2008;33:1135-1137.
126. Meinhardt-Wollweber M, Suhr C, Kniggendorf AK, Roth B. Tissue phantoms for multimodal approaches: Raman spectroscopy and optoacoustics. *Proc SPIE*.2014;8945:89450B.
127. Bergholt MS, Duraipandian S, Zheng W, Huang ZW. Multivariate reference technique for quantitative analysis of fiber-optic tissue Raman spectroscopy. *Anal Chem*. 2013;85:11297-11303.
128. Keren S, Zavaleta C, Cheng Z, de la Zerda A, Gheysens O, Gambhir SS. Noninvasive molecular imaging of small living subjects using Raman spectroscopy. *Proc Natl Acad Sci USA*. 2008;105:5844-5849.
129. Bohndiek SE, Wagadarikar A, Zavaleta CL, et al. A small animal Raman instrument for rapid, wide-area, spectroscopic imaging. *Proc Natl Acad Sci USA*. 2013;110:12408-12413.
130. Rodrigues M, Weersink RA, Whelan WM. Assessment of thermal coagulation in ex-vivo tissues using Raman spectroscopy. *J Biomed Opt*. 2010;15:068001.
131. Moody AS, Baghernejad PC, Webb KR, Sharma B. Surface enhanced spatially offset Raman spectroscopy detection of neurochemicals through the skull. *Anal Chem*. 2017;89:5689-5693.
132. Iping Petterson IE, Esmonde-White FWL, de Wilde W, Morris MD, Ariese F. Tissue phantoms to compare spatial and temporal offset modes of deep Raman spectroscopy. *Analyst*. 2015;140:2504-2512.
133. Sekar SKV, Mosca S, Farina A, et al. Frequency offset Raman spectroscopy (FORS) for depth probing of diffusive media. *Opt Express*. 2017;25:4585-4597.
134. Maher JR, Matthews TE, Reid AK, Katz DF, Wax A. Sensitivity of coded aperture Raman spectroscopy to analytes beneath turbid biological tissue and tissue-simulating phantoms. *J Biomed Opt*. 2014;19:117001.
135. Srinivasan S, Schulmerich M, Cole JH, et al. Image-guided Raman spectroscopic recovery of canine cortical bone contrast in situ. *Opt Express*. 2008;16:12190-12200.
136. Khan KM, Krishna H, Majumder SK, Rao KD, Gupta PK. Depth-sensitive Raman spectroscopy combined with optical coherence tomography for layered tissue analysis. *J Biophotonics*. 2014;7:77-85.
137. Khan KM, Majumder SK, Gupta PK. Cone-shell Raman spectroscopy (CSRS) for depth-sensitive measurements in layered tissue. *J Biophotonics*. 2015;8:889-896.
138. Mo JH, Zheng W, Huang ZW. Fiber-optic Raman probe couples ball lens for depth-selected Raman measurements of epithelial tissue. *Biomed Opt Express*. 2010;1:17-30.
139. Wang JF, Bergholt MS, Zheng W, Huang ZW. Development of a beveled fiber-optic confocal Raman probe for enhancing in vivo epithelial tissue Raman measurements at endoscopy. *Opt Lett*. 2013;38:2321-2323.
140. Sharma B, Ma K, Glucksberg MR, Van Duyne RP. Seeing through bone with surface-enhanced spatially offset Raman spectroscopy. *J Am Chem Soc*. 2013;135:17290-17293.
141. Filippou V, Tsoumpas C. Recent advances on the development of phantoms using 3D printing for imaging with CT, MRI, PET, SPECT, and ultrasound. *Med Phys*. 2018;45:E740-E760.